communications physics

A Nature Portfolio journal

Article

https://doi.org/10.1038/s42005-025-02162-6

Ultracold long-range van der Waals Rydberg trimers

Mateo Londoño [1] ✉, Vanessa C. Olaya-Agudelo [2], Felipe Herrera[2] & Jesús Pérez-Ríos[1]

Rydberg molecules are an essential ingredient of cold molecular sciences. Due to the richness of interactions between Rydberg atoms and neutral atoms, new kinds of Rydberg molecules and binding mechanisms are still to be discovered. In this work, we predict the existence of long-range van der Waals trimers in dilute atom-gas mixtures. These are bound states of a Rydberg atom and a diatomic polar molecule mediated by the long-range van der Waals interaction. This binding mechanism gives rise to trimers with sizes between 5 and 500 nm and binding energies between 0.2 kHz and 2 MHz depending on the atomic principal quantum number n and orbital angular momentum L. We show that these trimers can be produced via two-photon photoassociation, with rates on the order of (10^{-13} - 10^{-11}) cm^3s^{-1} for temperatures in the range of (0.5 μK - 10 μK), and discuss the feasibility of observing trimer resonances.

Rydberg atoms play a pivotal role in several areas of atomic, molecular, and optical physics (AMO)[1], such as the implementation of novel quantum information protocols[2], quantum simulation of many-body Hamiltonians[3], the study of impurity physics, non-linear quantum optics, and ultracold chemistry[4–6]. Many of these applications rely on controlling the exaggerated properties of Rydberg states in order to tailor the resulting interatomic forces. For example, at high densities, Rydberg excitations present a unique lineshape as a consequence of the Rydberg electron-perturber atom interaction[7,8], leading to, under appropriate conditions, the formation of ultralong-range Rydberg molecules[9,10,10–18], and possible polaron effects considering the Rydberg atom as an impurity in a dense atomic reservoir.[19–21] Another key ingredient in AMO physics is cold molecules, an essential platform for exploring fundamental quantum phenomena, such as the control of interactions in quantum chemistry[6,22], novel quantum phases[23–25], and quantum information processing[26]. Long-range interactions and state preparation make molecules ideal platforms for simulating complex quantum systems and advancing quantum technology applications.

Rydberg atoms interacting with cold molecules offer a unique opportunity for studying exotic Rydberg molecules. For instance, a Rydberg excitation in a dense gas of polar molecules, such that molecules can be found within the orbit of the Rydberg electron, can lead to the formation of long-range Rydberg trimer bound states primarily via the charged-dipole interaction between the Rydberg or core and the molecule plus elastic electron-molecule collisions[27–29]. In this scenario, the Rydberg electron scattering off the diatomic molecule establishes the binding mechanism. Similarly, when the Rydberg excitation is induced in a molecular gas, it gives rise to the formation of Rydberg bimolecules, an ultralong-range Rydberg molecule in which a molecular ionic core is bound to a molecule (inside the Rydberg orbit). These exotic molecules show large binding energies in the GHz regime and exhibit kilo-Debye permanent dipole moments[30]. A similar scenario has been proposed as a technique for sympathetic cooling of molecules[31].

In this work, we predict the existence of a long-range Rydberg trimer molecule when a Rydberg atom binds to a diatomic polar molecule via the van der Waals interaction. The Van der Waals interaction, responsible for the bonding in these trimers, dominates when the Rydberg-molecule distance is larger than the Le-Roy Radius, i.e., the distance beyond which electronic overlap is negligible. The considered long-range van der Waals potential is shown in Fig. 1, upper part of panel (b), while the gray shaded region represents the short-range potential, which is not considered here. These trimers will appear in a regime where the molecular density is much lower than the density of Rydberg atoms, so that at most one molecule resides within the Rydberg blockade radius r_B, but outside the Rydberg orbit r_n, as displayed in panel (a) of Fig. 1. This regime is complementary to previously reported ultralong-range Rydberg molecules, where the oscillatory Born-Oppenheimer potentials due to the Rydberg electron-perturber scattering appear below the Le-Roy radius[27,32]. The observation of a long-range van der Waals Rydberg trimer requires a two-photon photoassociation scheme starting from the ground electronic state of the atom and the molecule. This methodology is usually employed on the study of exotic Rydberg molecules involving Rydberg atoms in the S and D states. In analogy to the lineshape of Rydberg excitations in atomic gases[1], the two-photon photoassociation lineshape spectra will show traces of the existence of long-range van der Waals Rydberg trimers. Furthermore, studying these trimers will help better understand Rydberg-molecule interactions for molecular cooling[33] and polar molecule manipulation techniques[34–36].

[1]Department of Physics and Astronomy, Stony Brook University, Stony Brook, NY, 11794, USA. [2]Department of Physics, Universidad de Santiago de Chile, Santiago, 9170124, Chile. ✉e-mail: mateo.londoo@stonybrook.edu

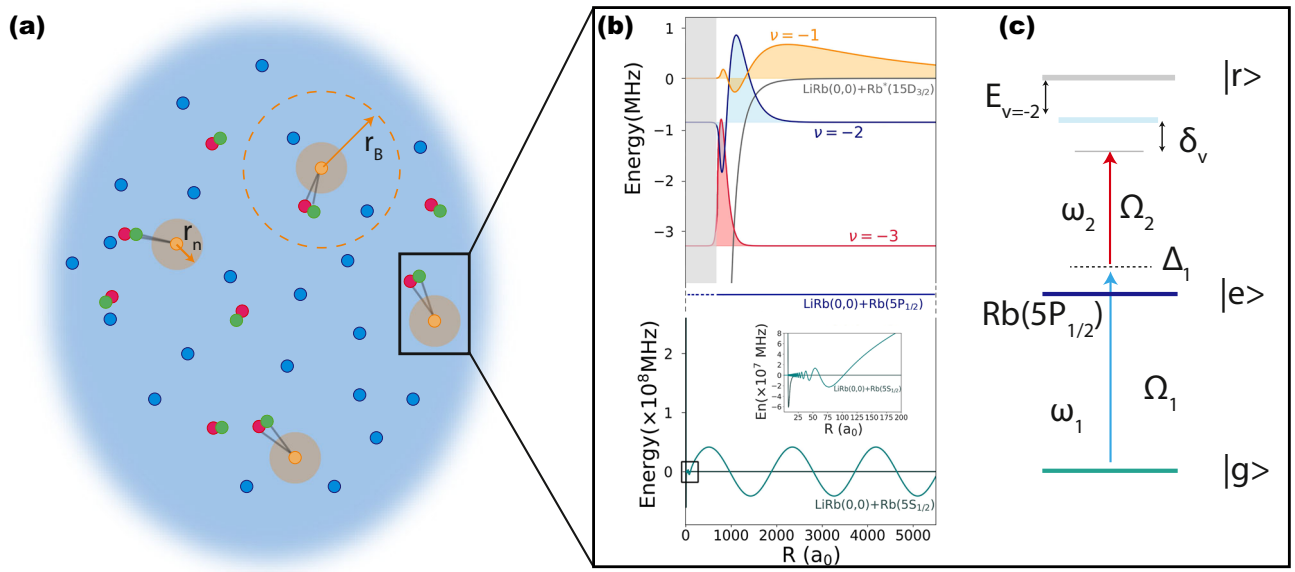

Fig. 1 | Formation of ultralong-range Rydberg trimers. Panel **a** shows a scheme of the atomic and molecular diluted gases, where not more than a single molecule can be found within the Rydberg blockade radius r_B, but outside the Rydberg electron orbit radius r_n. The Rydberg atoms are represented in orange, the neutral atoms in blue and the diatomic molecules in red and green. The zoom-in panels (**b**, **c**) show an example of interacting channels and potentials involved in the phtoassociation process for a given atom-molecule pair (Rb + LiRb). The relevant scattering and bound-state wavefunctions are shown in panel (**b**), where the inset shows a zoom-in of the initial continuum wavefunction, while the gray shaded area indicates the short-range part, not considered in this work. The process efficiency depends on the overlap between the initial scattering state [LiRb(0,0) + Rb($5^2S_{1/2}$)] and the final near-threshold vibrational state of the electronically excited trimer [LiRb(0,0) + Rb*($15^2D_{3/2}$)] ($|\Omega| = 3/2$), which exhibits three vibrational levels. The substantial difference of van der Waals lengths between the initial and final states is highlighted. Furthermore, the two-photon scheme for exciting alkali-metal atoms into a target Rydberg state is displayed in panel (**c**), where atomic states $|g\rangle, |e\rangle, |r\rangle$ are connected through the lasers ω_1 and ω_2, giving the two-photon detuning $\delta_\nu = \omega_1 + \omega_2 - (\omega_r - E_\nu)$) from the trimer bound level E_ν. Large intermediate detunings Δ_1 from the excited atomic level prevent gas heating via light scattering.

Results

Let us consider a mixed thermal gas consisting of atoms X, and molecules AB, in their ground vibrational state. A two-photon excitation, resonant with a Rydberg state of the atom X*, induces the following light-assisted chemical reaction known as two-photon photoassociation (PA)[37]:

$$\mathrm{X} + \mathrm{AB} + 2\gamma \rightarrow \mathrm{X}^* - \mathrm{AB}\,, \tag{1}$$

where $\mathrm{X}^* - \mathrm{AB}$ represents an excited trimer resonant with an excited electronic state that correlates with the atomic Rydberg state of the atom. These excited states are the long-range van der Waals trimers, and their existence is contingent to the nature of the long-range van der Waals $\mathrm{X}^* + \mathrm{AB}$ interaction and the reaction rate of Eq. (1).

We consider our atom as ^{85}Rb($5^2S_{1/2}$) and our molecule is either LiRb or KRb in the ground rovibrational state ($^1\Sigma^+, v = 0, J = 0$) since both of these molecules are available in the cold and ultracold regimes[38–40], although further efforts are still required to achieve a pure ground-state gas of LiRb. The Rydberg state of the atom is denoted as n^2L_j, where L is the atomic orbital angular momentum and j is the total electronic angular momentum. The initial state of the PA process is a scattering atom+molecule state denoted $|\Psi_l(E_{\mathrm{kin}})\rangle$, with collision energy E_{kin} and partial wave l, in the ground atom-molecule channel $|5^2S_{1/2}\rangle|X^1\Sigma^+\rangle$. Here, we assume an s-wave collision between the Rydberg atom and the molecule, i.e., $l = 0$. The final state of the process $|\Psi_\nu\rangle$ corresponds to the νth bound state of the trimer potential that correlates with the $|n^2L_j\rangle|X^1\Sigma^+\rangle$ asymptote. In addition, we consider the total angular momentum projection along the quantization axis $|\Omega = m + M| = 3/2$, where m is the atomic angular momentum projection $M = 0$ since we consider the molecule in the ground rotational state[41]. Here, we follow the usual labeling for vibrational states $\nu = -1, -2, -3, \ldots$, where $\nu = -1$ denotes the shallowest bound state.

For distances beyond the Le Roy radius of the Rydberg atom R_{LR}[42], the Rydberg-molecule interaction is given by the van der Waals term $V(r) = -C_6/r^6$, where r is the Rydberg-molecule distance. In many cases, this interaction has been shown to be attractive[41], so it can support bound states depending on the magnitude C_6. Figure 2a shows the dissociation energy of the Rydberg-molecule interaction potential as a function of the atomic principal quantum number n for all the species being considered. Therefore, bound state energies will span between 0.2 kHz and 20 MHz. We computed the number of bound states for each species using the Wentzel–Kramers–Brillouin (WKB) approximation, and the results agree with exact numerical calculations as shown in panels (b) and (c) of Fig. 2. Highly excited n-states have a larger Le Roy radius, which reduces the effective range of the attractive van der Waals force. As a result, the potential well becomes shallower, limiting the number of bound states. The C_6 coefficient, which depends on the molecular structure, is an order of magnitude larger for LiRb than for KRb, explaining the observed difference in the number of bound states. For example, for Rb*($15D_{1/2}$), the van der Waals coefficients are $C_6(\mathrm{LiRb}) = -2.778 \times 10^8$ a.u, and $C_6(\mathrm{KRb}) = -1.351 \times 10^7$ a.u. The Le Roy radius is the same in both cases, approximately 712 a_0.

We compute PA rates for $15 \le n \le 50$ Rydberg levels in the $^2S_{1/2}$ and $^2D_{3/2}$ atomic channels, but the formalism can be equally applied to other atomic and molecular states, provided the C_6 coefficients in the initial and final states are known. From resonance scattering theory[37,43], the PA rate

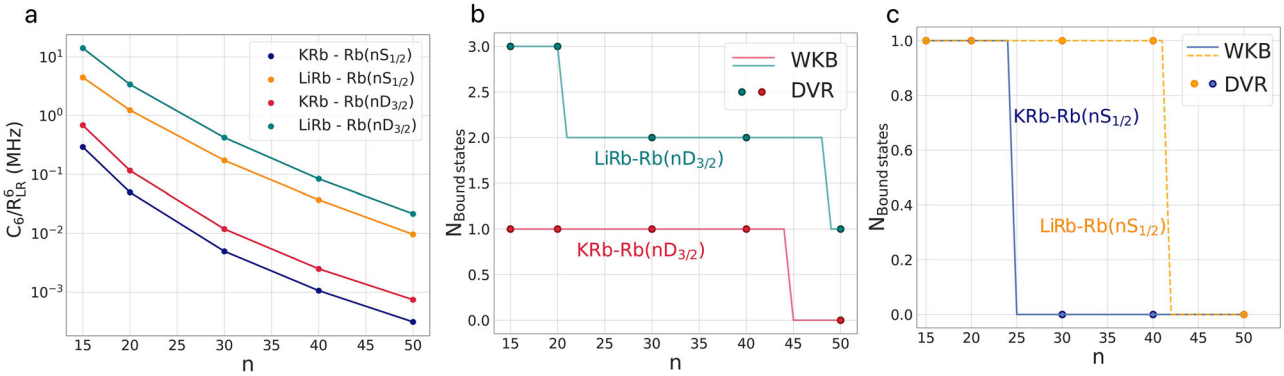

Fig. 2 | Characterization of the long-range Rydberg-molecule energy landscape. Panel **a** shows the dissociation energy of the trimer, it means, the Van der Waals potential evaluated at the minimum distance R_{LR}, as a function of the principal quantum number n.The different colors represent the various molecule-atom pairs. The curve follows a scaling law proportional to n^{-5} or n^{-6} depending on the Rydberg state see Ref. 41. Panels **b**, **c** show the number of bound states for each Rydberg-molecule potential, corresponding to the D and S states, respectively. The bound states were computed using the Wentzel–Kramers–Brillouin (WKB) approximation and the discrete variable representation (DVR) method. Both panels show the results as a function of the principal quantum number and the species considered.

constant can be written as

$$K_{PA}(E_{\rm kin}) = v_{\rm rel}\frac{\pi}{k^2}\sum_{l=0}^{\infty}(2l+1)|S_\nu(E_{\rm kin},l)|^2, \tag{2}$$

where $v_{\rm rel} = \sqrt{8k_BT/\pi\mu}$ is the relative velocity of the particles in the entrance channel, μ is the reduced mass of the Rydberg atom-molecule system, and $k = \sqrt{2\mu k_BT/\hbar^2}$ is the channel wavevector. k_B is the Boltzmann's constant and T is the temperature. The rate constant is determined by the element of the S-matrix that connects the scattering state and the bound state, given by[37]

$$|S_\nu(E_{\rm kin},l)|^2 = \frac{\gamma\,\Gamma_\nu(E_{\rm kin},l)}{[E_{\rm kin}/\hbar+\delta_\nu]^2+[\Gamma_T/2]^2}, \tag{3}$$

where $\delta_\nu = \omega_1+\omega_2-(E_a-E_\nu)$ is the two-photon detuning from the final state $|\Psi_\nu\rangle$, where E_a is the energy of the $Rb^*(n^2L_j)$ + Diatom ($X^1\Sigma^+$, $v=0$, $J=0$) asymptote, and E_ν is the binding energy of the ν-th near-threshold bound state. We can neglect the possible light shifts of these resonance frequencies for weak laser dressing fields. The two-photon excitation scheme is further specified in Fig. 1 (Panel c) in terms of the individual Rabi frequencies Ω_1 and Ω_2 of the driving lasers at ω_1 and ω_2, respectively. The derivation of the effective two-level approximation used in Eq. (3) is given in the "Methods" section.

The width of the scattering resonance in Eq.(3) depends on the overall decay rate of the atom-molecule trimer state, given by $\Gamma_T = \gamma = +\Gamma_\nu(E_{\rm kin},l)$, where γ is the natural linewidth of the Rydberg state and the stimulated absorption rate is given by:

$$\Gamma_\nu(E_{\rm kin},l) = 2\pi|V_\nu(E_{\rm kin},l)|^2, \tag{4}$$

where

$$V_\nu(E_{\rm kin},l) = \frac{\Omega_{\rm eff}}{2}\langle\Psi_\nu|\Psi_l(E_{\rm kin})\rangle. \tag{5}$$

Here, $\langle\Psi_\nu|\Psi_l(E_{\rm kin})\rangle$ represent the overlap between the initial scattering wavefunction and the final bound state wavefunction. For loosely bound vibrational states, it is a good approximation to neglect the radial dependence of the electric transition dipole moment, leading to an effective two-photon Rabi frequency of $\Omega_{\rm eff} = \Omega_1\Omega_2/2\Delta_1$ (more details in Ref. 44 and in the "Methods" section).

The bound state trimer wavefunctions were computed using the mapped Fourier Grid Hamiltonian method, incorporating a repulsive barrier as a numerical technique to explore long-range interactions of the system, without involving short-range effects ("Methods"). The initial scattering wavefunction was obtained using the Numerov method. With this information at hand, we compute the stimulated absorption coefficients for LiRb-$Rb^*(15\,D_{3/2})$ and LiRb-$Rb^*(20\,D_{3/2})$. The results are shown in Fig. 3 assuming the following Rydberg dressing parameters: $\Delta_1 = 80$ MHz, $\Omega_1 = 10$ MHz and $\Omega_2 = 8$ MHz associated to laser intensities $I_1 = 10^{-4}$ W/cm^2 and $I_2 = 1.5$ W/cm^2 at frequencies ω_1 and ω_2, respectively. The stimulated absorption rates are rather smooth except for certain dips due to the energy-dependent oscillatory nature of the continuum wavefunction, which affects its overlap with a given bound wavefunction, as Fig. 4 illustrates. Notably, the peak amplitude of the bound state $v=-3$ aligns with a node of the $E_k = 21$ μK scattering wavefunction, resulting in minimal overlap and producing the dip observed in panel (a) of Fig. 3. In contrast, the other two kinetic energies correspond to nonzero amplitudes at the $v=-3$ peak position, leading to a larger stimulated absorption rate (see panel (a) of Fig. 3).

Panel (c) of Fig. 3 displays the average stimulated absorption rate for LiRb + $Rb^*(nD_{3/2})$, including the contributions from all available bound states. The results are shown as a function of the collision energy, displaying a smooth behavior. For a given collision energy, the estimated absorption rate can be very distinct depending on the bound state under consideration, as highlighted in Fig. 4. Supplementary Tables 1 and 2, show a detailed study of the stimulated absorption rate for different molecular species and atomic quantum numbers.

We compute the two-photon PA lineshape profile for the LiRb-Rb(15 $D_{3/2}$), and the results are shown in Fig. 5. This figure displays the PA rate as a function of the two-photon detuning with respect to the least bound state associated with the LiRb-Rb(15 $D_{3/2}$) asymptote. The spectral overlap closely resembles the Lorentzian profile from Eq. (3) due to the low energy values of the bound states relative to the kinetic energy. This causes all peaks to appear tightly centered around $\delta_\nu = 0$. A closer examination of the spectrum, as shown in panel (b), reveals a more intricate structure where each bound state contributes uniquely. It is important to note that the peak intensity of each contribution varies with the collision energy. The width of the PA spectra shows the expected inverse proportionality of the spectrum broadening with the temperature, as in panel (a) of Fig. 5. An exhaustive list of the values of $K_{\rm PA}$ for the rest of bound states at the present temperatures is reported in Supplementary Tables 3 and 4.

Finally, we report the PA rate peak for four different Rydberg-molecule combinations as a function of the principal quantum number, and the results are shown in Fig. 6. Independently of the species under consideration, the PA peak rate constant varies from 10^{-13} to 10^{-11} cm^3 s^{-1}. Clearly, systems involving Rydberg atoms in the D state outperform those with a Rydberg in the S state since the former shows larger C_6 coefficients. It seems

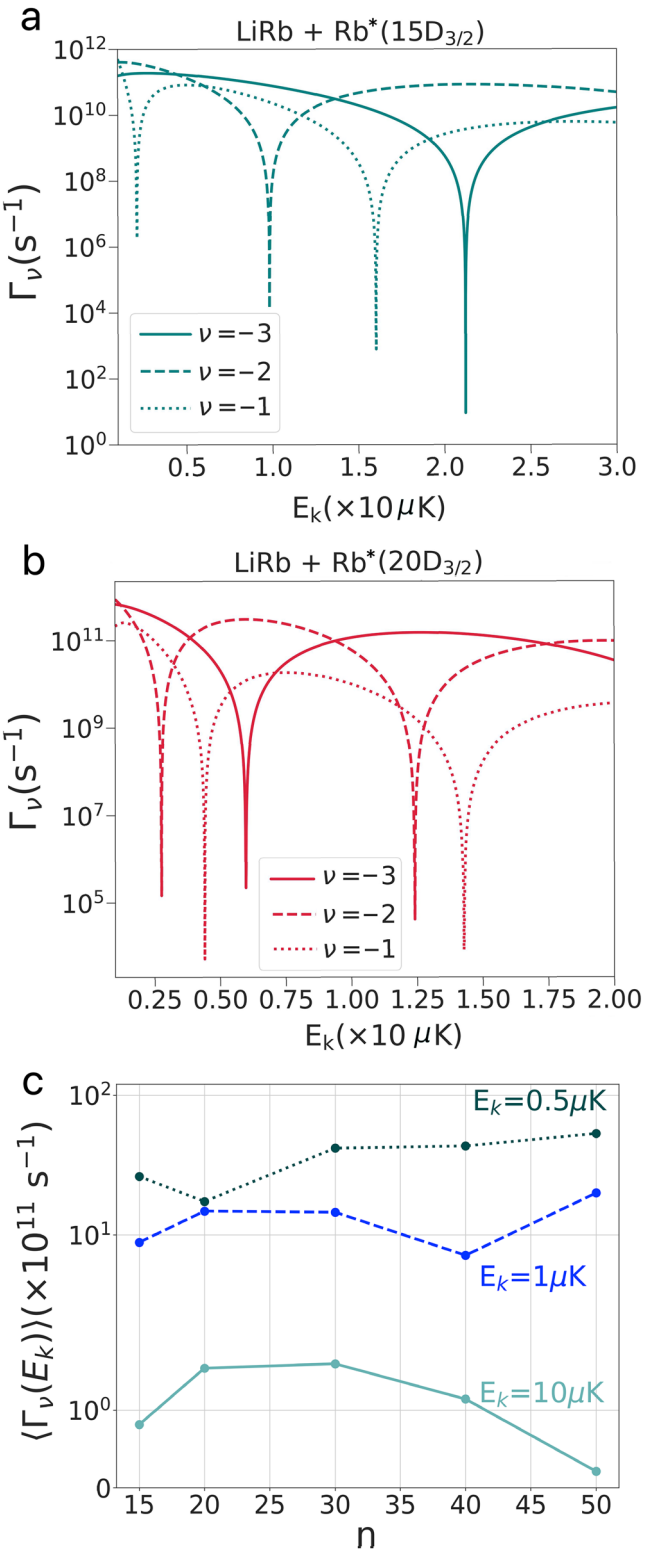

Fig. 3 | Stimulated Absorption rates as a function of the kinetic energy of the (LiRb + Rb*) collision pair. Panel **a** presents the stimulated absorption rates for Rb*($15D_{3/2}$) state. The different bound states contributions from $\nu = -3$, -2 and -1 are shown in teal solid, dashed and dotted lines, respectively. Similarly, Panel **b** shows same stimulated absorption rates for the Rb*($20D_{3/2}$) state, where the bound states contributions are shown in red with the same line style code as before. Panel **c** is the average absorption rate, over available bound states as a function of the principal quantum number n for LiRb + Rb*($nD_{3/2}$). Collision energies of 0.5, 1, and 10 μK are presented in green dotted, blue dashed and teal solid lines, respectively.

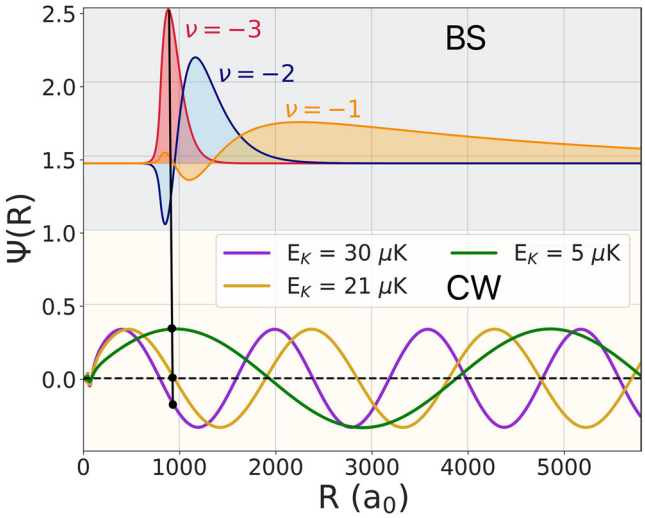

Fig. 4 | Overlap of the wavefunctions for computing the photoassociation rates. The upper region (gray background) shows the bound-state (BS) wavefunctions for the LiRb + Rb*($15D_{3/2}$) system. Three bound states exist in the potential, labeled by $\nu = -3$ (red), -2 (blue), and -1 (orange). The lower region (yellow background) displays the continuum wavefunctions (CW) corresponding to different collision energies, as indicated in the legend. The horizontal black dashed line marks the zero amplitude of the collisional wavefunctions, while the vertical black solid line highlights the vertical transitions—and thus the overlap—between the continuum states and the bound states.

that low principal quantum number states favor the PA rate toward the formation of long-range Van der Waals Rydberg trimers, which arises from the dependence of the S-matrix elements on the bound state energies and the Franck-Condon factors [Eq. (3)]. The absence of bound states for sufficiently large n values (Fig. 2) is consistent with previous observations in the Rb* + KRb system, in the context of inner-orbital long-range Rydberg trimers[28].

Discussion

We predict that long-range van der Waals Rydberg trimers exist in nature. The extension of these exotic trimers spans from 5 to 500 nm, depending on the atomic principal quantum number n and orbital quantum number L. The size is comparable to other exotic Rydberg molecules such as trilobite and butterfly molecules[9,11,12,14,15,45]. Using the width of the PA absorption spectrum, We estimate the lifetime of the trimer states to range from 10^{-9} to 10^{-4} s, indicating that they could be synthesized in the lab via two-photon PA. However, the lifetime can be reduced due to collisional effects between the molecules and the Rydberg atoms.

To discuss the feasibility of observing these new exotic Rydberg molecules, first, we consider the stimulated absorption rate, which in our case is $\sim 10^{12}\ s^{-1}$. The same magnitude for bi-alkali molecules via PA is of $1.5 \times 10^8\ s^{-1}$ for RbCs[46] and $3.5 \times 10^7\ s^{-1}$ for LiRb[38], using PA laser intensities on the order of 10^2–10^3 W/cm^2 and a temperature of ~100 μK. These examples also involve species that interact via van der Waals forces, but with values of C_6 that are several orders of magnitude smaller than our case. In addition, the PA process in these bi-alkali systems occurs at relatively short distances[37], which makes the process more sensitive to the details of the initial scattering wavefunction. Therefore, the predicted stimulated absorption rate is indicative that the photoassociation between a Rydberg atom and a diatomic polar molecule into a long-range van der Waals Rydberg molecule is somewhat efficient.

To observe long-range van der Waals Rydberg trimers, we propose to work in a regime where the molecular density is much smaller than the density of Rydberg atoms, such that there is at most one molecule residing within the Rydberg blockade radius r_B. The Rydberg radius depends on the

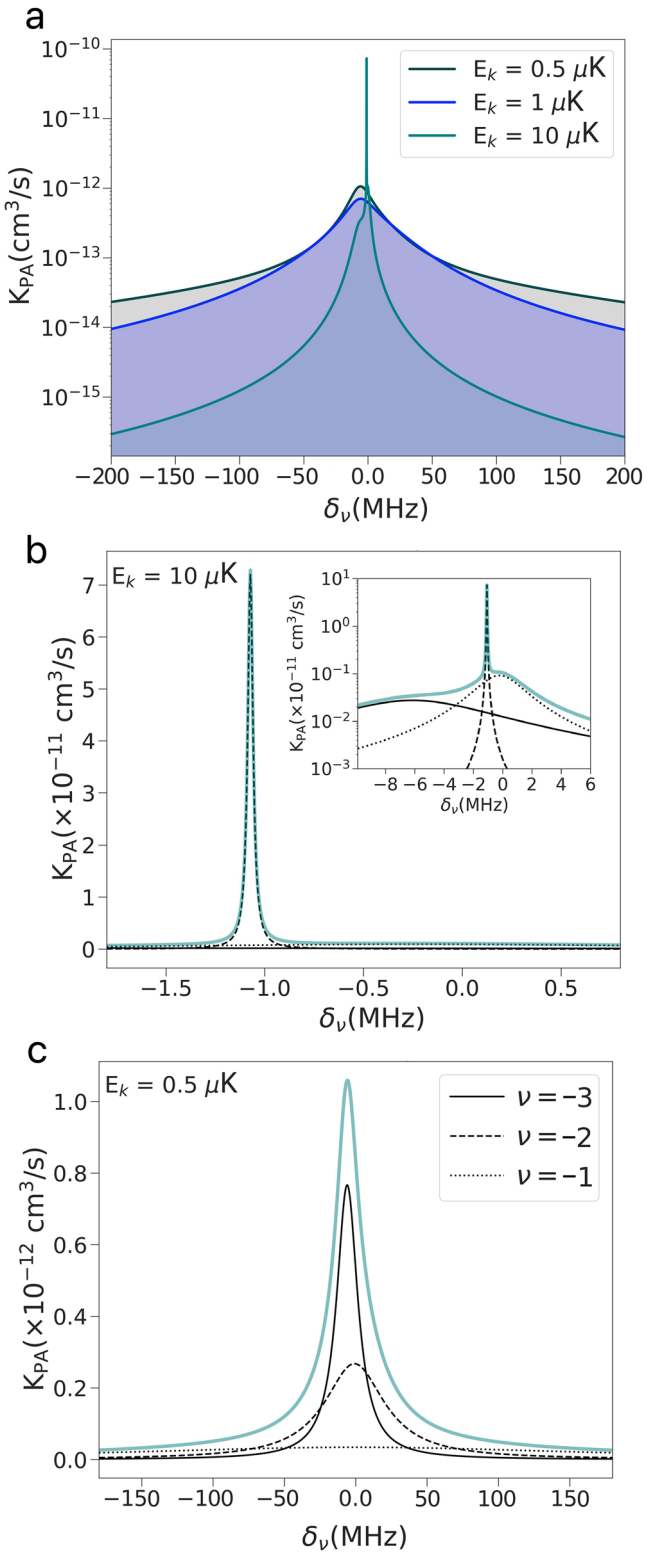

Fig. 5 | Photoassociation (PA) lineshape for LiRb+Rb*(15 $D_{3/2}$) for different collision energies. Panel **a** shows the PA lineshape for three collision energies: $E_k = 0.5$ μK (green), $E_k = 1$ μK (blue), $E_k = 10$ μK (teal). Panels **b**, **c** are the K_{PA} constants for $E_k = 10$ μK and 500 nK, respectively, including the contributions from each vibrational state. The vibrational states $\nu = -3$, $\nu = -2$ and $\nu = -1$ contributions are represented by solid, dashed and dotted curves, respectively. The inset on panel **b** is a zoom-in of the PA peak. The color coding for panels **b** and **c** is the same: vibrational states are given in panel (**c**), and the total spectrum is in cyan.

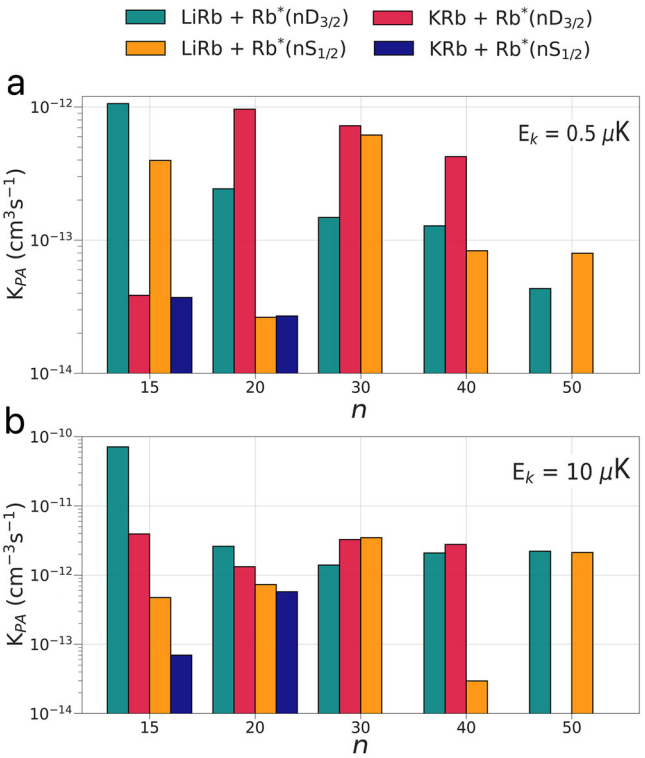

Fig. 6 | Peak photoassociation rates constant for LiRb-Rb* and KRb-Rb*. Panels **a**, **b** display the peak PA rate constants assuming a collision energy of 500 nK and 10 μK, respectively.

van der Waals interaction between the atoms in identical Rydberg levels[2]. Given a laser-dependent Rydberg excitation fraction $f < 1$, the critical ground atom density ρ_B below which we can ignore blockade effects can be estimated from $f \times \rho_B \times (4/3)\pi r_B^3 = 1$[1]. Assuming weak dressing $f \sim 10^{-2}$ and $r_B \sim 1$ μm[47], the relevant atom densities for this work $\rho_B \sim 10^{10}$ cm^{-3} are thus compatible with magneto-optical trapping[48,49]. Our molecule of choice is LiRb due to its strong long-range interaction and relatively large reduced mass. However, an ultracold degenerate gas of this molecule has yet to be achieved, although efficient short-range photoassociation pathways have been demonstrated for the triplet state[39]. Therefore, our work could be an incentive for efforts towards an ultracold gas of LiRb molecules.

In comparison with traditional cold-molecule formation experiments that target high-density molecular ensembles[50], our Rydberg trimer predictions could be tested in a low-density regime. Then, independent molecules are diluted in a background gas of alkali-metal atoms for atomic densities below the critical value beyond which Rydberg blockade effects become important[51], and thus aggregation effects between Rydberg atoms are suppressed[52]. On the other hand, ultralong-range van der Waals Rydberg trimers could be synthesized using optical tweezers. In this scenario, the molecule and atom are in adjacent tweezers, so the two-photon photoassociation profile is considered a function of the distance between the two tweezer traps. Thus, our work sets the foundations for a deeper understanding of the exotic properties of ultracold molecules in atomic Rydberg reservoirs.

Methods

Scattering and bound states wavefunctions

The initial scattering wavefunction was obtained by solving numerically the Schrödinguer equation describing the interaction of ground state LiRb(KRb) with ground state Rb. We solve the radial equation with the Numerov method, assuming a Lennard–Jones potential between the atom

and the molecule. This potential model accurately describes the long-range dispersion forces acting on the system at large distances where PA takes place. Note that for the assumed experimental conditions, rotational excitation leading to anisotropies does not play any role. For LiRb interacting with Rb, the Lennard-Jones parameters are $C_6 = 7159$ a.u, $D_e = 2036\ \mathrm{cm}^{-1}$ and $C_{12} = C_6^2/4D_e$, while for KRb interacting with Rb we have $C_6 = 8798$ a.u, $D_e = 1584\ \mathrm{cm}^{-1}$, with the same definition for C_{12}. Both sets of parameters are taken from Ref. 53.

Bound state wavefunctions $|\Psi_\nu\rangle$ are calculated using a mapped Fourier grid Hamiltonian method[54] given a Rydberg-molecule effective trimer potential. The Rydberg-molecule interaction potential is characterized by $V(R) = C_6/R^6$ up to $R = R_c$ where we impose a repulsive barrier to avoid further penetration. The discussed results were obtained using $R_c = 1.1R_{LR}$, where LeRoy radius is estimated from $R_{LR} \sim \sqrt{10}n^2a_0$. The convergence of the results was tested by varying the position of the barrier between R_{LR} and $1.2\,R_{LR}$. The relative deviation in the energy of threshold states, which are the most affected by the barrier position, ranges from 9% to 16%, scaling with the value of the Le Roy radius. Additionally, even without knowing the exact barrier position, we can confirm that the energy of the threshold bound state does not exceed the theoretical limit $E_{-1} \approx 39.5\,E_{\mathrm{vdW}}$ in the s-wave regime as outlined in Ref. 55. Here, $E_{\mathrm{vdW}} \equiv \sqrt{2}\hbar^3/\mu^{3/2}C_6^{1/2}$. As a specific example, for the highly excited LiRb + $Rb^*(50D_{3/2})$ state, the theoretical threshold-state energy is approximately 1.694×10^{-2} MHz, while the reported value we used is 1.062×10^{-2} MHz. The remaining bound states are generally farther from their respective theoretical limits. The obtained number of bound states coincides with analytical estimates from the WKB approximation which yields, for a given C_6 coefficient, a total number of bound states $N_{max} = \frac{1}{10n^4}\sqrt{\frac{\mu C_6}{2\pi^2}} + \frac{\pi}{4}$. Where the outer turning point is approximated to be at $R = \infty$ and the inner turning point is $R = R_{\mathrm{LR}}$.

Effective two-level system

The Hamiltonian that describes a three-level system, like the one shown in Fig. 1, is given by ($\hbar = 1$):

$$\begin{aligned} H =& \omega_e|e\rangle\langle e| + \omega_r|r\rangle\langle r| + \frac{\Omega_1}{2}\left[|g\rangle\langle e|e^{i\omega_1 t} + |e\rangle\langle g|e^{-i\omega_1 t}\right] \\ &+ \frac{\Omega_2}{2}\left[|e\rangle\langle r|e^{i\omega_2 t} + |r\rangle\langle e|e^{-i\omega_2 t}\right], \end{aligned} \tag{6}$$

where ω_e (ω_r) is the energy of the $|e\rangle$ ($|r\rangle$) state and the energy of $|g\rangle$ is set to zero. Ω_a and ω_a are the Rabi frequency and energy of the laser a, with $a = 1, 2$.

Using a unitary rotation frame transformation $U(t) = |g\rangle\langle g| + e^{i\omega_1 t}|e\rangle\langle e| + e^{i(\omega_1+\omega_2)t}|r\rangle\langle r|$, the interaction Hamiltonian can be written as[56]

$$\begin{aligned} H_I =& -\Delta_1|e\rangle\langle e| + \delta|r\rangle\langle r| \\ &+ \frac{\Omega_1}{2}\left[|g\rangle\langle e| + |e\rangle\langle g|\right] + \frac{\Omega_2}{2}[|e\rangle\langle r| + |r\rangle\langle e|], \end{aligned} \tag{7}$$

where $\delta = \omega_r - (\omega_1 + \omega_2)$ and $\Delta_1 = \omega_1 - \omega_e$. The time evolution of the system is determined by the Schrödinger equation $i\partial_t|\Psi\rangle = H_I|\Psi\rangle$, where $|\Psi(t)\rangle = c_g(t)|g\rangle + c_e(t)|e\rangle + c_r(t)|r\rangle$ is the system state. In the rotating frame, $|e\rangle$ has fast oscillations and instantaneously tends to a steady state compared with the slow motion of the rest of the system. Therefore, we assume that $\dot{c}_e = 0$. Thus, the equations of motion are given by:

$$i\dot{c}_g(t) = \frac{\Omega_1^2}{4\Delta_1}c_g(t) + \frac{\Omega_1\Omega_2}{4\Delta_1}c_r(t), \tag{8}$$

$$i\dot{c}_r(t) = \delta c_r(t) + \frac{\Omega_2^2}{4\Delta_1}c_r(t) + \frac{\Omega_1\Omega_2}{4\Delta_1}c_g(t). \tag{9}$$

Eqs. (8) and (9) are the same differential equation obtained from a two-level system with an effective Rabi frequency $\Omega_{\mathrm{eff}} = \frac{\Omega_1\Omega_2}{2\Delta_1}$ and an effective detuning.

$$\delta_{\mathrm{eff}} = \delta + \frac{\Omega_2^2}{4\Delta_1} - \frac{\Omega_1^2}{4\Delta_1}. \tag{10}$$

Data availability

The authors declare that the data supporting the findings of this study are available within the paper and its supplementary information files.

Received: 7 January 2025; Accepted: 26 May 2025;
Published online: 04 June 2025

References

1. Gallagher, T. F. *Rydberg Atoms*. 3 (Cambridge University Press, 2005).
2. Saffman, M., Walker, T. G. & Mølmer, K. Quantum information with Rydberg atoms. *Rev. Mod. Phys.* **82**, 2313–2363 (2010).
3. Browaeys, A. & Lahaye, T. Many-body physics with individually controlled Rydberg atoms. *Nat. Phys.* **16**, 132–142 (2020).
4. Schlagmüller, M. et al. Ultracold chemical reactions of a single Rydberg atom in a dense gas. *Phys. Rev. X* **6**, 031020 (2016).
5. Pérez-Ríos, J. *An Introduction to Cold and Ultracold Chemistry* (Springer International Publishing, 2020). https://www.ebook.de/de/product/39345358/jesus_perez_rios_an_introduction_to_cold_and_ultracold_chemistry.html.
6. Karman, T., Tomza, M. & Pérez-Ríos, J. Ultracold chemistry as a testbed for few-body physics. *Nat. Phys.* **20**, 722–729 (2024).
7. Liebisch, T. C. et al. Controlling Rydberg atom excitations in dense background gases. *J. Phys. B* **49**, 182001 (2016).
8. Scheuing, T. & Pérez-Ríos, J. Quasi-static lineshape theory for Rydberg excitations in high-density media. *Atoms* **11**, 95 (2023).
9. Greene, C. H., Dickinson, A. S. & Sadeghpour, H. R. Creation of polar and nonpolar ultra-long-range Rydberg molecules. *Phys. Rev. Lett.* **85**, 2458–2461 (2000).
10. Bendkowsky, V. et al. Observation of ultralong-range Rydberg molecules. *Nature* **458**, 1005–1008 (2009).
11. Hamilton, E. L., Greene, C. H. & Sadeghpour, H. R. Shape-resonance-induced long-range molecular Rydberg states. *J. Phys. B* **35**, L199–L206 (2002).
12. Khuskivadze, A. A., Chibisov, M. I. & Fabrikant, I. I. Adiabatic energy levels and electric dipole moments of Rydberg states of Rb_2 and Cs_2 dimers. *Phys. Rev. A* **66**, 042709 (2002).
13. Gaj, A. et al. From molecular spectra to a density shift in dense Rydberg gases. *Nat. Commun.* **5**, 4546 (2014).
14. Booth, D., Rittenhouse, S. T., Yang, J., Sadeghpour, H. R. & Shaffer, J. P. Production of trilobite Rydberg molecule dimers with kilo-debye permanent electric dipole moments. *Science* **348**, 99–102 (2015).
15. Niederprüm, T. et al. Observation of pendular butterfly Rydberg molecules. *Nat. Commun.* **7**, 12820 (2016).
16. Fey, C., Hummel, F. & Schmelcher, P. Ultralong-range Rydberg molecules. *Mol. Phys.* **118**, e1679401 (2020).
17. Shaffer, J. P., Rittenhouse, S. T. & Sadeghpour, H. R. Ultracold Rydberg molecules. *Nat. Commun.* **9**, 1965 (2018).
18. Eiles, M. T., Pérez-Ríos, J., Robicheaux, F. & Greene, C. H. Ultracold molecular Rydberg physics in a high density environment. *J. Phys. B* **49**, 114005 (2016).
19. Camargo, F. et al. Creation of Rydberg polarons in a Bose gas. *Phys. Rev. Lett.* **120**, 083401 (2018).
20. Sous, J., Sadeghpour, H. R., Killian, T. C., Demler, E. & Schmidt, R. Rydberg impurity in a Fermi gas: quantum statistics and rotational blockade. *Phys. Rev. Res.* **2**, 023021 (2020).

21. Durst, A. A. T. & Eiles, M. T. Phenomenology of a Rydberg impurity in an ideal Bose-Einstein condensate. *Phys. Rev. Res.* **6**, L042009 (2024).
22. Shammout, B., Karpa, L., Ospelkaus, S., Tiemann, E. & Dulieu, O. Modeling photoassociative spectra of ultracold nak+ k. *J. Phys. Chem. A* **127**, 7872–7883 (2023).
23. Bigagli, N. et al. Observation of Bose-Einstein condensation of dipolar molecules. *Nature* **631**, 289–293 (2023).
24. Langen, T. et al. Dipolar droplets of strongly interacting molecules. *Phys. Rev. Lett.* **134**, 053001 (2025).
25. Wenzel, M., Pfau, T. & Ferrier-Barbut, I. A fermionic impurity in a dipolar quantum droplet. *Phys. Scr.* **93**, 104004 (2018).
26. Cornish, S. L., Tarbutt, M. R. & Hazzard, K. R. A. Quantum computation and quantum simulation with ultracold molecules. *Nat. Phys.* **20**, 730–740 (2024).
27. Rittenhouse, S. T. & Sadeghpour, H. R. Ultracold giant polyatomic Rydberg molecules: coherent control of molecular orientation. *Phys. Rev. Lett.* **104**, 243002 (2010).
28. Aguilera-Fernández, J., Sadeghpour, H. R., Schmelcher, P. & González-Férez, R. Electronic structure of ultralong-range Rydberg penta-atomic molecules with two polar diatomic molecules. *Phys. Rev. A* **96**, 052509 (2017).
29. González-Férez, R., Rittenhouse, S. T., Schmelcher, P. & Sadeghpour, H. R. A protocol to realize triatomic ultralong range rydberg molecules in an ultracold krb gas. *J. Phys. B* **53**, 074002 (2020).
30. González-Férez, R., Shertzer, J. & Sadeghpour, H. R. Ultralong-range Rydberg bimolecules. *Phys. Rev. Lett.* **126**, 043401 (2021).
31. Zhang, C., Rittenhouse, S. T., Tscherbul, T. V., Sadeghpour, H. R. & Hutzler, N. R. Sympathetic cooling and slowing of molecules with Rydberg atoms. *Phys. Rev. Lett.* **132**, 033001 (2024).
32. Mellado-Alcedo, D., Guttridge, A., Cornish, S. L., Sadeghpour, H. R. & González-Férez, R. Ultralong-range Cs-RbCs Rydberg molecules: Nonadiabaticity of dipole moments. *Phys. Rev. A* **110**, 013314 (2024).
33. Zhao, B., Glaetzle, A. W., Pupillo, G. & Zoller, P. Atomic Rydberg reservoirs for polar molecules. *Phys. Rev. Lett.* **108**, 193007 (2012).
34. Zhang, C. & Tarbutt, M. Quantum computation in a hybrid array of molecules and Rydberg atoms. *PRX Quantum* **3**, 030340 (2022).
35. Gawlas, K. & Hogan, S. D. Rydberg-state-resolved resonant energy transfer in cold electric-field-controlled intrabeam collisions of nh3 with rydberg he atoms. *J. Phys. Chem. Lett.* **11**, 83–87 (2020).
36. Patsch, S., Zeppenfeld, M. & Koch, C. P. Rydberg atom-enabled spectroscopy of polar molecules via förster resonance energy transfer. *J. Phys. Chem. Lett.* **13**, 10728–10733 (2022).
37. Jones, K. M., Tiesinga, E., Lett, P. D. & Julienne, P. S. Ultracold photoassociation spectroscopy: long-range molecules and atomic scattering. *Rev. Mod. Phys.* **78**, 483–535 (2006).
38. Dutta, S., Lorenz, J., Altaf, A., Elliott, D. S. & Chen, Y. P. Photoassociation of ultracold LiRb* molecules: observation of high efficiency and unitarity-limited rate saturation. *Phys. Rev. A* **89**, 020702 (2014).
39. Blasing, D. B., Stevenson, I. C., Pérez-Ríos, J., Elliott, D. S. & Chen, Y. P. Short-range photoassociation of LiRb. *Phys. Rev. A* **94**, 062504 (2016).
40. Ni, K.-K. et al. A high phase-space-density gas of polar molecules. *Science* **322**, 231–235 (2008).
41. Olaya, V., Pérez-Ríos, J. & Herrera, F. C_6 coefficients for interacting Rydberg atoms and alkali-metal dimers. *Phys. Rev. A* **101**, 032705 (2020).
42. Le Roy, R. J. Theory of deviations from the limiting near-dissociation behavior of diatomic molecules. *J. Chem. Phys.* **73**, 6003–6012 (1980).
43. Bohn, J. L. & Julienne, P. S. Semianalytic theory of laser-assisted resonant cold collisions. *Phys. Rev. A* **60**, 414–425 (1999).
44. Browaeys, A., Barredo, D. & Lahaye, T. Experimental investigations of dipole–dipole interactions between a few Rydberg atoms. *J. Phys. B* **49**, 152001 (2016).
45. Giannakeas, P., Eiles, M. T., Robicheaux, F. & Rost, J. M. Dressed ion-pair states of an ultralong-range Rydberg molecule. *Phys. Rev. Lett.* **125**, 123401 (2020).
46. Kerman, A. J., Sage, J. M., Sainis, S., Bergeman, T. & DeMille, D. Production of ultracold, polar RBcs* molecules via photoassociation. *Phys. Rev. Lett.* **92**, 033004 (2004).
47. Singer, K., Stanojevic, J., Weidemüller, M. & Côté, R. Long-range interactions between alkali Rydberg atom pairs correlated to thens–ns,np–np andnd–nd asymptotes. *J. Phys. B* **38**, S295–S307 (2005).
48. Singer, K., Reetz-Lamour, M., Amthor, T., Marcassa, L. G. & Weidemüller, M. Suppression of excitation and spectral broadening induced by interactions in a cold gas of Rydberg atoms. *Phys. Rev. Lett.* **93**, 163001 (2004).
49. Tong, D. et al. Local blockade of Rydberg excitation in an ultracold gas. *Phys. Rev. Lett.* **93**, 063001 (2004).
50. Matsuda, K. et al. Resonant collisional shielding of reactive molecules using electric fields. *Science* **370**, 1324–1327 (2020).
51. Balewski, J. B. et al. Rydberg dressing: understanding of collective many-body effects and implications for experiments. *N. J. Phys.* **16**, 063012 (2014).
52. Schempp, H. et al. Full counting statistics of laser excited Rydberg aggregates in a one-dimensional geometry. *Phys. Rev. Lett.* **112**, 013002 (2014).
53. Mayle, M., Ruzic, B. P. & Bohn, J. L. Statistical aspects of ultracold resonant scattering. *Phys. Rev. A* **85**, 062712 (2012).
54. Kokoouline, V., Dulieu, O., Kosloff, R. & Masnou-Seeuws, F. Mapped fourier methods for long-range molecules: Application to perturbations in the Rb2(0u+) photoassociation spectrum. *J. Chem. Phys.* **110**, 9865–9876 (1999).
55. Gao, B. Zero-energy bound or quasibound states and their implications for diatomic systems with an asymptotic van der Waals interaction. *Phys. Rev. A* **62**, 050702 (2000).
56. Steck, D. A. *Quantum and Atom Optics* (Available online at http://steck.us/teaching, revision 0.13.4, 24 September 2020).

Acknowledgements

M.L.C. and J.P.-R. acknowledge the support from the Stony Brook OVPR seed program and the Simons Foundation. F.H. and V.O.-A. were supported by ANID through grants Fondecyt Regular 1221420 and Millennium Scientific Initiative ICN17_012.

Author contributions

M. Londoño completed the calculations and analysis of the results, produced the corresponding figures, and contributed to the manuscript preparation. V.C. Olaya-Agudelo initiated the calculations and developed the codes for computing stimulated absorption rates and photoassociation rate constants. F. Herrera and J. Pérez-Ríos contributed equally to the formulation and conceptualization of the project, as well as to the preparation of the paper. J. Pérez-Ríos also designed the scheme presented in Fig. 1.

Competing interests

The authors declare no competing interests. J. Pérez-Ríos is a Guest Editor for Communications Physics, but was not involved in the editorial review of, or the decision to publish this article.

Additional information

Supplementary information The online version contains supplementary material available at https://doi.org/10.1038/s42005-025-02162-6.

Correspondence and requests for materials should be addressed to Mateo Londoño.

Peer review information *Communications Physics* thanks the anonymous reviewers for their contribution to the peer review of this work. A peer review file is available.